Supplementary Information

Silver complex-modified tetravanadium-substituted polyoxomolybdates containing ordered tunnels for supercapacitors and electrocatalytic CO_2 reduction

Wufeng Zhang[a,1], Yuwen Wang[a,1], Liping Cui[a*], Meilin Wang[c], Kai Yu[a,b*]

Table of Contents

1.Experimental section..3

2.Structural figures...11

3.Structural data..13

4.Characterizationand and testing...18

5.Theoretical calculation..28

References...30

1. Experimental section

1.1 Material

Sodium molybdate dihydrate ($NaMoO_4 \cdot 2H_2O$, ≥99.0%), sodium arsenite ($NaAsO_2$, 98.0%), ammonium metavanadate (NH_4VO_3, 99.0%), 4,4'-Bipyridyl, ($C_{10}H_8N_2$, 98.0%), hydrochloric acid (HCl, 99.0%), silver nitrate ($AgNO_3$, ≥99.8%), potassium bicarbonate ($KHCO_3$, 99.7%), isopropyl alcohol (C_3H_8O, ≥99.5%) were used without any refinement. The reagents used were purchased from Sigma-Aldrich. Nafion solution (5 wt%, American DuPont). Activated carbon (AC), acetylene black (AB), and water-based cellulose separator (90 μm) were all purchased from Saibo electrochemical materials company.

1.2 Safety Precautions

All experimental operations involving arsenite precursors were conducted within chemical safety fume hoods. Personnel wore nitrile gloves, chemical-resistant goggles, and protective clothing throughout the process to avoid direct contact with precursors. Arsenic-containing waste generated during experiments was sorted and collected for centralized disposal by a third-party waste management company for non-hazardous treatment. Quantitative analysis of the recycled electrolyte using ICP-MS revealed an arsenic leaching concentration of only 0.002 μg/L. This level is significantly below both the World Health Organization's drinking water arsenic limit (10 μg/L) and China's National Comprehensive Wastewater Discharge Standard.

1.3 Material synthesis

1.3.1 **AMV-1:** A mixture of and $Na_2Mo_4 \cdot 2H_2O$ (0.7017 g, 2.90 mmol), $NaAsO_2$ (0.3767g, 2.90 mmol), NH_4VO_3 (0.2340 g, 2.00 mmol), 4,4'-Bipyridyl (0.2343 g, 1.50 mmol) and H_2O (20 mL) were stirred at room temperature for 30 minutes; then the pH value was adjusted to about 3 with 6 M HCl, and it was sealed in a 25-mL Teflon-lined stainless steel reactor, which was heated at 160 °C for 5 days. The blue crystals were isolated and collected by filtration, washed thoroughly with distilled water, and dried at room temperature (Yield: 45% based on Mo). The waste liquid of the reaction is collected and treated separately for the toxicity of sodium arsenite. Anal. Calcd. For $C_{20}H_{16}As_3Mo_8N_4O_{40}V_4$ (Mr = 2148.41): C, 11.19; H, 0.75; N, 2.61; As, 10.46; V, 9.48; O, 29.79; Mo, 35.72. Found: C, 11.21; H, 0.76; N, 2.6; As, 10.44; V, 9.49; O, 29.77; Mo, 35.73.

***1.3.2* AMV-2:** A mixture of and $Na_2Mo_4 \cdot 2H_2O$ (0.7379 g, 3.05 mmol), $NaAsO_2$ (0.3871 g, 2.98 mmol), $AgNO_3$ (0.1614 g，0.95 mmol), NH_4VO_3 (0.2398 g, 2.05 mmol), 4,4’-Bipyridyl (0.2265 g, 1.45 mmol) and H_2O (20 mL) were stirred at room temperature for 30 minutes; then the pH value was adjusted to about 3 with 6 M HCl, and it was sealed in a 25-mL Teflon-lined stainless steel reactor, which was heated at 160 °C for 5 days. The blue crystals were isolated and collected by filtration, washed thoroughly with distilled water, and dried at room temperature (Yield: 48% based on Mo). The waste liquid of the reaction is collected and treated separately for the toxicity of sodium arsenite. Anal. Calcd. For $C_{45}H_{38}Ag_2As_2Mo_8N_9O_{42}V_5$ (Mr = 2764.65): C, 19.56; H, 1.39; N, 4.56; As, 5.42; V, 9.21; Ag, 7.80; O, 24.30; Mo, 27.76. Found: C, 19.57; H, 1.37; N, 4.58; As, 5.41; V, 9.23; Ag, 7.81; O, 24.29; Mo, 27.74.

1.4 Materials characterization

1.4.1 Apparatus

Perkin-elmer 2400 CHN elemental analyzer was used for elemental analysis (C, H and N); As, Mo, V, Ag, were analyzed by ICP atomic emission spectrometer inplasma specification. Infrared spectra in the 500-4000 cm^{-1} range were recorded using KBr microspheres on a Centaurus FT/IR spectrophotometer. TG analysis was performed in flowing nitrogen gas at a heating rate of 10°C·min^{-1} on the Perkin Elmer TGA7 instrument. The XRD patterns were collected on Rigaku Dmax 2000 X-ray diffractometer, with graphite monochromatic Cu Kα radiation (SEM = 0.154 nm) and two apertures between 5 and 50°. NMR measurements were performed at Agilent MR400DD2 NMR spectrometer operating at 400 MHz. Samples were prepared by mixing 450 μL of the electrolyte solutions with 50 μL of D_2O.

1.4.2 X-ray crystallography

Single crystal X-ray data of compounds **1** and **2** were collected on a Bruker SMART CCD diffractometer equipped with graphite monochromatized MoKa radiation (λ = 0.71073 Å). Semiempirical absorption corrections were applied using the SADABS program. The structure was solved by direct method and refined by the full-matrix least-squares methods on F^2 using the SHELXTL-2014 software package. All of the non-hydrogen atoms were refined anisotropically. Hydrogen atoms on carbon atoms of organic ligands were included at calculated positions and refined with a riding model. The H atoms on water molecules were not included and just put into the final molecular formula. A summary of crystal data and structure refinement for compounds **1-2** were provided in Table S1. Selected bond lengths and angles for compounds **1-2** are listed in Table S2, and S3. Crystallographic data for the structures have been deposited in the Cambridge Crystallographic Data Centre. CCDC numbers of compounds **1-2** are 2219731 and 2219732, respectively.

1.5 Electrode preparation

1.5.1 **Preparation of GCE**: The glassy carbon electrode (GCE) working electrode was polished before each experiment with 1, 0.3, and 0.05 mm alumina power on chamois leather, respectively, rinsed horoughly with deionized water between each polishing step. To prepare the working electrode, a mixture of the **1** or **2**, and reduced graphene oxide (rGO) in a weight ratio of 1:1 was ground in a mortar with 1 mL of ethyl alcohol, and 3 mL of DI water and was as the solvent to make slurry. 5 μL of well dispersed slurry was dropped onto the glassy carbon with a diameter of 3 mm and dried for 2 hours at room temperature, in order to form a uniform thin film. The mass of the active material on each electrode is approximately 1 mg/cm^2. Then, 5 μL of Nafion solution was dropped onto the GCE surface and the electrode was then dried at room temperature.

1.5.2 **Preparation of AMV-2-CPE:** The working electrodes were made by mixing as-synthesized compound, rGO and PVDF (5:5:1) in N-methyl pyrrolidinone, and grinding the compounds for about 30 min to form a slurry, which was then coated on carbon paper (1 cm^2) and dried at 60 ℃ for 12 h. The mass of the active material on each electrode is approximately 1 mg/cm^2.

1.5.3 **Preparation of ASC device:** The ASC device was prepared by using **AMV-2-**CPE as negative electrode and activated carbon (AC) as the positive one. The AC electrode was prepared by pressing a homogeneous paste of 80 % (wt.) active carbon, 10 % (wt.) acetylene black and 10 % (wt.) PVDF onto carbon paper followed by overnight drying at 60 ℃. 0.5 M H_2SO_4 solutions were used as the electrolyte, and a porous filter paper as the separator.

1.5.4 **Preparation of CO_2RR Preparation of working electrodes:**

3.5 mg acetylene black, 8 mg crystal, and 0.5% Nafion solution (160 μL) were dispersed in 480 μL of 1:1 water/isopropyl alcohol mixture. In order to mix evenly, the mixture needs to be treated with ultrasound for more than 30 minutes. Then, drop the mixture (60 μL × 2) on both sides of the carbon paper (1 cm × 1 cm). The mass of the active material on each electrode is approximately 0.65 mg/cm^2.

1.6 Electrochemical measurements

1.6.1 Supercapacitor Performance Measurement

The electrochemical performance of CHI 660E electrochemical workstation was evaluated with 1- and 2-based modified glass carbon electrode (GCE) and carbon paper electrode (CPE) were used as working electrodes respectively in a three-electrode system of 0.25 $mol \cdot L^{-1}$ H_2SO_4, Ag/AgCl was used as a reference electrode and a Pt wire was acted as the counter electrode and in a double-electrode system with carbon paper impregnated with activated carbon as cathode material. Cyclic voltammetry (CV) was tested at room temperature at scanning rates of 20, 40, 60, 80, 100, 120, 140, 160, 180, and 200 $mV \cdot s^{-1}$ for GCE and 10, 20, 30, 40, 50, 60, 70, 80, 90, and 100 $mV \cdot s^{-1}$ for CPE. At current densities of 2, 4, 6, 8, 10 $A \cdot g^{-1}$ for GCE of three-electrode system, and 2, 4, 6, 8, 10 $A \cdot g^{-1}$ for CPE of three-electrode system, the galvanostatic charge-discharge (GCD) performances were experimented. Electrochemical impedance spectroscopy (EIS) tests were conducted on this apparatus at the frequency from 0.01 Hz to 100 kHz. The specific capacitance (Cs) was computed with the equation below: $Cs = I\Delta t/m\Delta V$ and $Ca = I\Delta t/SV$ where I (A) refer to the current in the course of the discharge, Δt (s) means the time of discharge, m (g) is the mass of the electrode materials, and ΔV (V) is the voltage difference between the upper and lower potential limits, S (cm^2) is the geometrical area of the electrode.

The calculation formula of the pseudocapacitor contribution path is as follows:

$$\mathrm{i} = a\nu^{b}$$

$$\log \mathrm{i} = \mathrm{b} \log \nu + \log \mathrm{a}$$

In the CV test, at different voltage sweep rates (v, mV/s), different peak current values (i, mA) were obtained. If the value of b is in the range of 0.5-1, the electrode material exhibits battery properties and pseudocapacitive properties.

$$\mathrm{i(V)}/\nu^{1/2} = \mathrm{k_1}\nu^{1/2} + \mathrm{k_2}$$

Where υ is a specific voltage sweep speed, V is a specified voltage, k_1 and k_2 are adjustable parameters, and each specific voltage corresponds to a fitted value of k_1. At each specific voltage, $k_1υ$ is the pseudocapacitance contribution to the current.

The charge balance of the positive and negative electrodes was adjusted by controlling the loading amount of the active materials by using the following relationship

$M^+/M^-=(C^-\times V^-)/(C^+\times V^+)$

in which M^+, C^+, and V^+ are the mass of active material, the gravimetric specific capacitance, and the potential window of the AC electrode and M^-, C^-, and V^- are the mass of active material, the gravimetric specific capacitance, and the potential widow of the **AMV-2** electrode. The total mass of positive and negative electrode materials was about 3 mg.

$C=I\times \Delta t / (V\times m)$

in which I [A] is the constant discharge current, m [kg] is the active mass, V [V] is the potential window during the discharge process after the IR drop, and t [s] is the discharge time. For three-electrode measurements, the specific capacitance values are calculated based on the mass of the active material on the working electrode only. For the asymmetric supercapacitor (ASC) device, including the reported specific capacitance, energy density, and power density, all values are calculated based on the total mass of active materials on both the positive and negative electrodes, following standard practice in supercapacitor device evaluation.

The energy density E [Wh kg^{-1}] and power density P [W kg^{-1}] arecomputed according to Equation：

$E = C\Delta V^2 / 7.2$

in which C [F g^{-1}] is the gravimetric specific capacitance calculated from the discharge curve and V [V] is the potential window during the discharge process.

$P = 3600E / \Delta t$

in which E is the energy density and t is the discharge time.

1.6.2 **CO_2RR Electrocatalytic test:**

Electrocatalysis experiments of all catalysts were performed on the electrochemical workstation (CHI600E) in a standard three-electrode configuration in 0.5 m $KHCO_3$ (pH = 7.2). Pt sheet and Ag/AgCl were used as reference electrode and counter electrode, respectively, and modified carbon paper (1 cm^2) was used as work electrode. The electrochemical CO_2RR performance was performed in an airtight electrochemical H-type cell, two compartments were separated by an exchange membrane (Nafion 117). The polarization curves were tested by LSV measurement with a scan rate of 5 mV s^{-1} (iR-correction 100%). Polarization curves of the modified electrodes were recorded in Ar-saturated and CO_2-saturated $KHCO_3$ solution in sequence. The EIS measurements were made at -0.8 V (vs RHE). In this study, the solution resistance was determined using the built-in electrochemical impedance spectroscopy (EIS) method of the electrochemical workstation. A small-amplitude AC signal was applied to the electrochemical system over a frequency range of 0.01–

100,000 Hz. The solution resistance (R_s) was directly obtained from the high-frequency intercept of the impedance spectrum. In order to estimate the ECSA, cyclic voltammograms were tested by measuring double-layer capacitance (C_{dl}) under the potential window of 0 to -0.1 V (vs Ag/AgCl) with various scan rates from 20 to 160 mV s^{-1}. In this work, all the potentials were measured versus Ag/AgCl electrode and the results were reported versus RHE based on the Nernst equation: E (vs RHE) = E (vs Ag/AgCl) + 0.1989 V + 0.059 × pH.

The electrolyte solution in the cathodic compartment was stirred at 500 rpm, while CO_2 was continuously purged into the solution at a flow rate of 20 mL min^{-1}, regulated via a throttle valve. Electrolysis was conducted at applied potentials ranging from -0.6 V to -1.2 V vs. RHE. The gaseous products from the reaction were directed into the gas-sampling loop of a gas chromatograph (Shimadzu) for composition analysis. Hydrogen (H_2) was quantified using a thermal conductivity detector, and carbon monoxide (CO) was analyzed with a flame ionization detector equipped with a methanizer. Concentrations of the gaseous products were determined based on the integral area ratio of each component to the corresponding standard, using single-component calibration gases. All experiments were performed in triplicate, and the average values were used for subsequent calculations.

The liquid products were collected from the cathode chambers after electrolysis and quantified by NMR (Bruker AVANCEAV III 400) spectroscopy, in which 0.5 mL electrolyte was mixed with 0.1 mL D_2O and 0.1 μL dimethyl sulfoxide (DMSO, 99.99%, internal standard). Solvent pre-saturation technique was implemented to suppress the water peak.

The faradic efficiency was calculated as follow:

$$\mathrm{FE}(\%) = \frac{Q_{\mathrm{production}}}{Q_{\mathrm{totalcharge}}} \times 100\% = \frac{\frac{1\ \mathrm{mL}}{22.4\ L/mol} \times Y \times N \times F}{\mathrm{i} \times \frac{1\ mL}{v} \times 60\ s/min}$$

Where Y is the concentration of CO or H_2 in a 1 mL sample loop based on calibration of the GC with a standard gas, N is the number of electrons required to form a molecule of CO or H_2, F is the Faraday constant, and i is the recorded current, ν is the flow rate of CO_2.

Partial current density for CO (j_{CO}) was calculated by

$$j_{\mathrm{CO}} = j_{\mathrm{total}} \times \mathrm{FE}_{\mathrm{CO}}$$

where j_{total} is the total current density normalized to the geometric area of the electrode, and $\mathrm{FE}_{\mathrm{CO}}$ is the Faradaic efficiency of CO product determined by gas chromatography. All electrochemical data were normalized to this geometric area.

2. Structural figures

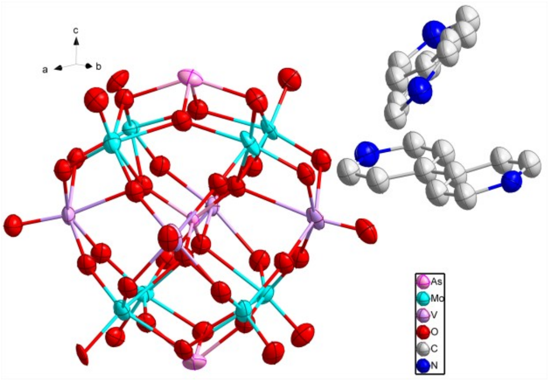

Figure S1. The ORTEP view of the basic units of AMV-1 with 50% thermal ellipsoids.

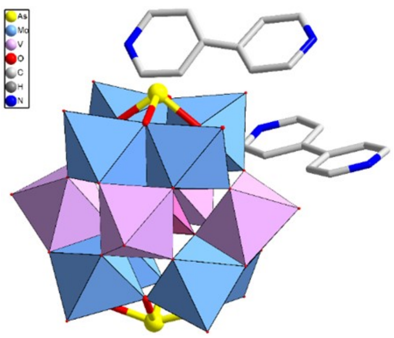

Figure S2. Monomer diagram of AMV-1.

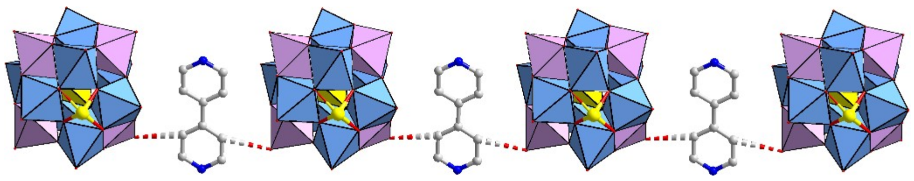

Figure S3. One-dimensional wavy chain formation of $\{As^{III}_2AsMo_8V_4O_{40}\}$ polyanion and bipy via supramolecular forc.

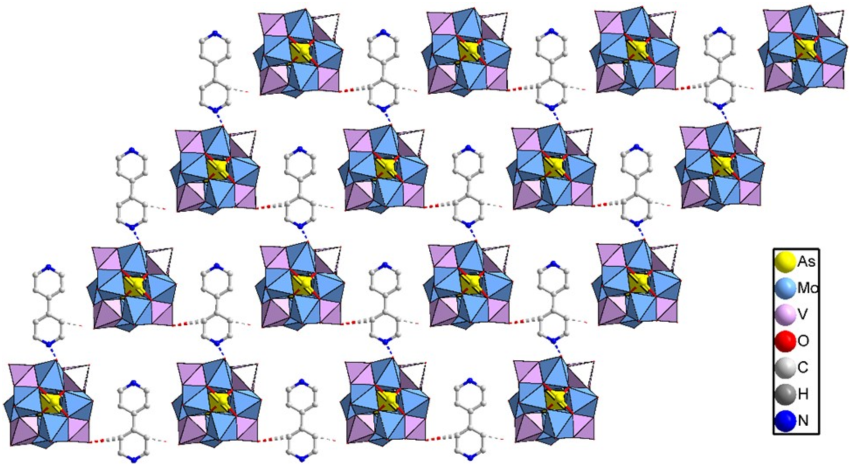

Figure S4. Regular 2D supramolecular lamellae formed by one-dimensional chains.

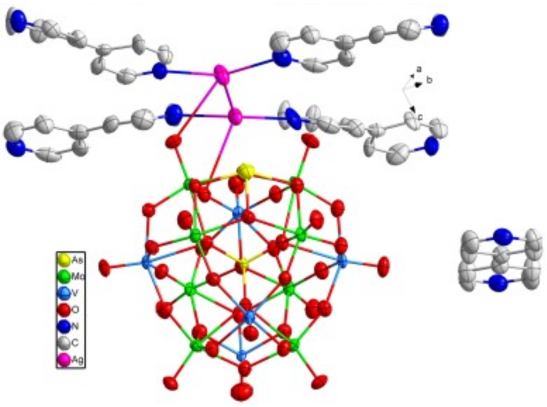

Figure S5. (a) Monomer diagram of AMV-2; (b) The ORTEP view of the basic units of AMV-2 with 50% thermal ellipsoids;

3. Structural data

Table S1. Crystal data and structure refinements for AMV-1 and AMV-2.

Compound	1	2
Chemical formula	$C_{20} H_{16} As_3 Mo_8 N_4 O_{40} V_4$	$C_{45} H_{38} Ag_2 As_2 Mo_8 N_9 O_{42}$
Mr	2148.41	2764.65
T/K	296(2)	295(2)
Crystal system	Monoclinic	Monoclinic
Space group	Cc	P2(1)/c
a/Å	15.366(11)	21.538(3)
b/Å	21.297(17)	13.5842(15)
c/Å	21.649(16)	25.303(3)
α/°	90	90
β/°	97.317(13)	99.858(4)
γ/°	90	90
V/Å^3	7027(9)	7293.6(15)
Z	4	4
D_{calc}/Mg m^{-3}	2.031	2.518
μ/mm^{-1}	3.363	3.457
F（000）	4044	5316
crystal size/mm	0.167 x 0.153 x 0.143	0.176 x 0.164 x 0.158
θ range/°	1.643- 24.996	2.218- 26.081
Reflections collected/	11895 / 11853 [R(int) =	98423 / 14425 [R(int) =
Data/restraints/paramete	11853 / 1506 / 664	14425 / 955 / 1036
R_1/ wR_2 [I ≥ 2σ（I）]^a	0.0863/0.1993	0.0583/0.1155
R（F）/wR（F^2）^{a}	0.0959/0.2013	0.0908/0.1236
GOF on F^2	1.087	1.092
Δρfin （max/min）, e	2.111 / -2.136	1.849 / -1.953
Compound	1	2

$^aR_1 = \Sigma||F_o| - |F_c||/\Sigma|F_o|$; $^bwR_2 = \Sigma[w(F_o^2 - F_c^2)^2]/\Sigma[w(F_o^2)^2]^{1/2}$.

Table S2. Selected bond lengths (Å) and bond angles (º) of AMV-1.

Bond	Dist.	Bond	Dist.	Bond	Dist.
Mo(1)-O(1)	2.02(3)	Mo(2)-O(1)	2.11(3)	Mo(3)-O(2)	2.09(3)
Mo(1)-O(5)	2.15(3)	Mo(2)-O(2)	2.13(3)	Mo(3)-O(3)	1.76(3)
Mo(1)-O(15)	1.87(2)	Mo(2)-O(16)	2.40(3)	Mo(3)-O(4)	2.04(3)
Mo(1)-O(16)	2.38(3)	Mo(2)-O(29)	1.84(3)	Mo(3)-O(13)	2.37(3)
Mo(1)-O(21)	1.71(2)	Mo(2)-O(31)	1.66(3)	Mo(3)-O(25)	1.83(3)
Mo(1)-O(22)	1.78(3)	Mo(2)-O(32)	1.73(3)	Mo(3)-O(38)	1.81(3)
Mo(4)-O(4)	2.06(3)	Mo(5)-O(6)	2.10(3)	Mo(6)-O(6)	2.11(3)
Mo(4)-O(5)	2.10(3)	Mo(5)-O(9)	2.11(3)	Mo(6)-O(7)	2.10(3)
Mo(4)-O(12)	1.80(3)	Mo(5)-O(10)	1.79(3)	Mo(6)-O(18)	1.61(3)

Mo(4)-O(13)	2.35(3)	Mo(5)-O(14)	1.73(3)	Mo(6)-O(28)	2.40(3)
Mo(4)-O(23)	1.77(3)	Mo(5)-O(28)	2.35(3)	Mo(6)-O(34)	1.74(2)
Mo(4)-O(40)	1.88(3)	Mo(5)-O(30)	1.78(3)	Mo(6)-O(37)	1.82(3)
Mo(7)-O(7)	2.11(3)	Mo(8)-O(8)	2.01(3)	V(1)-O(10)	1.98(3)
Mo(7)-O(8)	2.13(3)	Mo(8)-O(9)	2.14(3)	V(1)-O(11)	1.64(3)
Mo(7)-O(17)	1.70(3)	Mo(8)-O(24)	1.78(3)	V(1)-O(12)	1.96(3)
Mo(7)-O(27)	1.69(3)	Mo(8)-O(26)	1.85(3)	V(1)-O(13)	2.34(3)
Mo(7)-O(33)	2.40(3)	Mo(8)-O(36)	1.68(3)	V(1)-O(26)	1.91(3)
Mo(7)-O(39)	1.73(3)	V(3)-O(20)	1.61(2)	V(1)-O(38)	1.99(3)
V(2)-O(15)	1.96(3)	V(3)-O(21)	2.04(3)	V(4)-O(24)	2.03(3)
V(2)-O(17)	2.03(3)	V(3)-O(28)	2.31(3)	V(4)-O(25)	1.99(3)
V(2)-O(19)	1.51(3)	V(3)-O(30)	2.00(3)	V(4)-O(32)	1.98(3)
V(2)-O(29)	2.00(3)	V(3)-O(34)	2.08(3)	V(4)-O(33)	2.36(3)
V(2)-O(37)	1.92(3)	V(3)-O(40)	1.88(3)	V(4)-O(35)	1.55(3)
As(1)-O(13)	1.74(3)	As(2)-O(1)	1.99(3)	V(4)-O(39)	2.07(3)
As(1)-O(16)	1.60(3)	As(2)-O(2)	1.83(3)	As(3)-O(6)	2.01(3)
As(1)-O(28)	1.72(3)	As(2)-O(4)	2.03(3)	As(3)-O(7)	1.88(3)
As(1)-O(33)	1.64(3)	As(2)-O(5)	1.74(3)	As(3)-O(8)	2.12(3)
As(3)-O(9)	1.79(3)				

Angle	（°）	Angle	（°）	Angle	（°）
O(21)-Mo(1)-O(1)	148.6(12)	O(31)-Mo(2)-O(1)	91.8(13)	O(3)-Mo(3)-O(2)	101.5(12)
O(21)-Mo(1)-O(5)	82.2(11)	O(31)-Mo(2)-O(2)	96.9(13)	O(3)-Mo(3)-O(4)	102.7(12)
O(21)-Mo(1)-O(15)	102.5(11)	O(31)-Mo(2)-O(16)	161.2(12)	O(3)-Mo(3)-O(13)	172.0(11)
O(21)-Mo(1)-O(16)	88.1(11)	O(31)-Mo(2)-O(29)	104.1(14)	O(3)-Mo(3)-O(25)	98.7(13)
O(21)-Mo(1)-O(22)	100.4(12)	O(31)-Mo(2)-O(32)	110.8(14)	O(3)-Mo(3)-O(38)	100.6(13)
O(23)-Mo(4)-O(4)	98.3(12)	O(10)-Mo(5)-O(6)	151.5(10)	O(18)-Mo(6)-O(6)	97.8(13)
O(23)-Mo(4)-O(5)	92.2(12)	O(10)-Mo(5)-O(9)	86.7(11)	O(18)-Mo(6)-O(7)	105.7(13)
O(23)-Mo(4)-O(12)	113.9(12)	O(10)-Mo(5)-O(14)	101.6(12)	O(18)-Mo(6)-O(28)	165.7(11)
O(23)-Mo(4)-O(13)	166.9(11)	O(10)-Mo(5)-O(28)	86.6(11)	O(18)-Mo(6)-O(34)	94.6(13)
O(23)-Mo(4)-O(40)	102.1(12)	O(10)-Mo(5)-O(30)	98.7(13)	O(18)-Mo(6)-O(37)	107.0(13)
O(17)-Mo(7)-O(7)	85.9(11)	O(36)-Mo(8)-O(8)	93.0(12)	O(11)-V(1)-O(10)	103.4(13)
O(17)-Mo(7)-O(8)	154.1(11)	O(36)-Mo(8)-O(9)	99.4(12)	O(11)-V(1)-O(12)	100.5(13)
O(17)-Mo(7)-O(27)	105.1(13)	O(36)-Mo(8)-O(24)	103.9(14)	O(11)-V(1)-O(13)	169.8(13)
O(17)-Mo(7)-O(33)	87.2(11)	O(36)-Mo(8)-O(26)	108.0(12)	O(11)-V(1)-O(26)	104.4(13)
O(17)-Mo(7)-O(39)	98.1(13)	O(20)-V(3)-O(21)	104.0(13)	O(11)-V(1)-O(38)	99.0(13)
O(19)-V(2)-O(15)	104.8(15)	O(20)-V(3)-O(28)	165.5(13)	O(35)-V(4)-O(24)	102.5(15)
O(19)-V(2)-O(17)	97.2(14)	O(20)-V(3)-O(30)	100.1(12)	O(35)-V(4)-O(25)	101.2(14)
O(19)-V(2)-O(29)	98.2(13)	O(20)-V(3)-O(34)	94.7(12)	O(35)-V(4)-O(32)	102.8(16)
O(19)-V(2)-O(37)	105.5(14)	O(20)-V(3)-O(40)	109.6(13)	O(35)-V(4)-O(33)	172.8(15)
O(33)-As(1)-O(13)	108.9(9)	O(5)-As(2)-O(1)	79.8(11)	O(35)-V(4)-O(39)	102.8(13)
O(33)-As(1)-O(16)	110.4(14)	O(5)-As(2)-O(2)	105.2(14)	O(9)-As(3)-O(6)	78.6(12)
O(33)-As(1)-O(28)	116.7(15)	O(5)-As(2)-O(4)	77.6(13)	O(9)-As(3)-O(7)	103.1(13)
O(9)-As(3)-O(8)	78.4(11)				

Table S3. Selected bond lengths (Å) and bond angles (º) of AMV-2.

Bond	Dist.	Bond	Dist.	Bond	Dist.
Mo(1)-O(6)	1.795(6)	Mo(2)-O(1)	2.085(6)	Mo(3)-O(7)	2.078(6)
Mo(1)-O(12)	2.117(6)	Mo(2)-O(11)	1.819(6)	Mo(3)-O(15)	2.158(6)
Mo(1)-O(26)	1.832(6)	Mo(2)-O(16)	1.772(6)	Mo(3)-O(20)	1.786(5)
Mo(1)-O(31)	2.393(6)	Mo(2)-O(21)	1.686(6)	Mo(3)-O(23)	1.789(6)
Mo(1)-O(34)	2.073(6)	Mo(2)-O(25)	2.091(6)	Mo(3)-O(29)	2.369(6)
Mo(1)-O(35)	1.691(6)	Mo(2)-O(30)	2.375(6)	Mo(3)-O(40)	1.689(6)
Mo(4)-O(2)	2.072(6)	Mo(5)-O(1)	2.077(6)	Mo(6)-O(2)	2.067(6)
Mo(4)-O(13)	1.769(6)	Mo(5)-O(4)	1.755(6)	Mo(6)-O(3)	1.775(6)
Mo(4)-O(17)	1.796(6)	Mo(5)-O(5)	1.808(6)	Mo(6)-O(10)	1.813(6)
Mo(4)-O(22)	2.380(5)	Mo(5)-O(14)	1.696(6)	Mo(6)-O(22)	2.399(6)
Mo(4)-O(25)	2.079(6)	Mo(5)-O(28)	2.092(6)	Mo(6)-O(28)	2.100(6)
Mo(4)-O(32)	1.681(6)	Mo(5)-O(30)	2.397(6)	Mo(6)-O(37)	1.687(6)
Mo(7)-O(8)	1.793(6)	Mo(8)-O(7)	2.085(6)	V(1)-O(3)	1.964(6)
Mo(7)-O(15)	2.158(6)	Mo(8)-O(9)	1.788(6)	V(1)-O(4)	1.997(6)
Mo(7)-O(18)	1.787(6)	Mo(8)-O(12)	2.090(6)	V(1)-O(8)	1.974(6)
Mo(7)-O(29)	2.385(5)	Mo(8)-O(27)	1.802(6)	V(1)-O(23)	1.983(6)
Mo(7)-O(33)	1.709(5)	Mo(8)-O(31)	2.368(6)	V(1)-O(24)	1.594(6)
Mo(7)-O(34)	2.082(6)	Mo(8)-O(38)	1.689(6)	V(1)-O(29)	2.456(6)
V(2)-O(5)	1.973(6)	V(3)-O(9)	1.955(6)	V(4)-O(13)	1.962(6)
V(2)-O(6)	1.937(6)	V(3)-O(10)	1.982(6)	V(4)-O(16)	1.962(6)
V(2)-O(11)	1.990(6)	V(3)-O(17)	1.978(6)	V(4)-O(26)	1.988(6)
V(2)-O(18)	1.939(6)	V(3)-O(20)	1.934(6)	V(4)-O(27)	1.961(6)
V(2)-O(19)	1.581(6)	V(3)-O(22)	2.400(6)	V(4)-O(31)	2.360(6)
V(2)-O(30)	2.391(6)	V(3)-O(39)	1.579(6)	V(4)-O(36)	1.589(6)
V(5)-O(7)	1.886(6)	Ag(1)-N(7)#4	2.695(11)	Ag(3)-N(6)	2.657(12)
V(5)-O(12)	1.970(6)	Ag(1)-N(5)#2	2.698(11)	Ag(3)-N(8)	2.716(11)
V(5)-O(15)	2.033(7)	As(1)-O(22)	1.681(5)	Ag(2)-N(3)	2.783(14)
V(5)-O(34)	1.890(6)	As(1)-O(29)	1.658(5)	Ag(2)-N(4)	2.698(13)
V(5)-O(41)	1.582(7)	As(1)-O(30)	1.682(6)	Ag(2)-O(12)	2.815(12)
As(2)-O(2)	2.018(6)	As(1)-O(31)	1.682(6)	As(2)-O(1)	1.998(5)
As(2)-O(25)	1.865(6)	As(2)-O(28)	1.856(6)		

Angle	（°）	Angle	（°）	Angle	（°）
O(35)-Mo(1)-O(6)	105.6(3)	O(21)-Mo(2)-O(1)	96.9(3)	O(40)-Mo(3)-O(7)	98.6(3)
O(35)-Mo(1)-O(12)	97.9(3)	O(21)-Mo(2)-O(11)	103.7(3)	O(40)-Mo(3)-O(15)	95.0(3)
O(35)-Mo(1)-O(26)	101.8(3)	O(21)-Mo(2)-O(16)	106.0(3)	O(40)-Mo(3)-O(20)	105.5(3)
O(35)-Mo(1)-O(31)	164.5(3)	O(21)-Mo(2)-O(25)	96.4(3)	O(40)-Mo(3)-O(23)	101.7(3)
O(35)-Mo(1)-O(34)	99.4(3)	O(21)-Mo(2)-O(30)	166.2(3)	O(40)-Mo(3)-O(29)	163.3(2)
O(32)-Mo(4)-O(2)	98.5(3)	O(14)-Mo(5)-O(1)	98.6(3)	O(37)-Mo(6)-O(2)	98.6(3)
O(32)-Mo(4)-O(13)	104.9(3)	O(14)-Mo(5)-O(4)	104.0(3)	O(37)-Mo(6)-O(3)	104.1(3)
O(32)-Mo(4)-O(17)	103.2(3)	O(14)-Mo(5)-O(5)	101.9(3)	O(37)-Mo(6)-O(10)	102.0(3)
O(32)-Mo(4)-O(22)	167.3(3)	O(14)-Mo(5)-O(28)	100.5(3)	O(37)-Mo(6)-O(22)	166.5(3)
O(32)-Mo(4)-O(25)	98.4(3)	O(14)-Mo(5)-O(30)	166.6(2)	O(37)-Mo(6)-O(28)	99.8(3)
O(33)-Mo(7)-O(8)	101.7(3)	O(38)-Mo(8)-O(7)	98.8(3)	O(24)-V(1)-O(3)	103.8(3)
O(33)-Mo(7)-O(15)	95.6(3)	O(38)-Mo(8)-O(9)	105.1(3)	O(24)-V(1)-O(4)	103.2(3)
O(33)-Mo(7)-O(18)	106.0(3)	O(38)-Mo(8)-O(12)	96.8(3)	O(24)-V(1)-O(8)	101.7(3)
O(33)-Mo(7)-O(29)	163.5(3)	O(38)-Mo(8)-O(27)	102.3(3)	O(24)-V(1)-O(23)	102.2(3)

O(33)-Mo(7)-O(34)	99.0(3)	O(38)-Mo(8)-O(31)	164.7(3)	O(24)-V(1)-O(29)	169.1(3)
O(19)-V(2)-O(5)	99.8(3)	O(39)-V(3)-O(9)	103.2(3)	O(36)-V(4)-O(13)	104.5(3)
O(19)-V(2)-O(6)	104.6(3)	O(39)-V(3)-O(10)	101.6(3)	O(36)-V(4)-O(16)	103.0(3)
O(19)-V(2)-O(11)	100.5(3)	O(39)-V(3)-O(17)	101.7(3)	O(36)-V(4)-O(26)	98.7(3)
O(19)-V(2)-O(18)	103.0(3)	O(39)-V(3)-O(20)	103.1(3)	O(36)-V(4)-O(27)	101.0(3)
O(19)-V(2)-O(30)	169.3(3)	O(39)-V(3)-O(22)	170.7(3)	O(36)-V(4)-O(31)	168.4(3)
O(41)-V(5)-O(7)	121.6(3)	O(29)-As(1)-O(22)	108.6(3)	O(28)-As(2)-O(1)	80.1(2)
O(41)-V(5)-O(12)	107.3(4)	O(29)-As(1)-O(30)	108.8(3)	O(28)-As(2)-O(2)	79.8(2)
O(41)-V(5)-O(15)	107.0(3)	O(29)-As(1)-O(31)	110.2(3)	O(28)-As(2)-O(25)	110.7(3)
O(41)-V(5)-O(34)	124.5(3)	N(7)#4-Ag(1)-N(5)#2	112.0(4)	N(4)-Ag(2)-N(3)	110.7(4)
N(6)-Ag(3)-N(8)	117.4(4)	N(7)#4-Ag(1)-Ag(3)	105.3(3)	N(4)-Ag(2)-O(12)	105.7(4)
N(6)-Ag(3)-Ag(1)	111.7(4)				

Symmetry transformations used to generate equivalent atoms: #1 -x,-y,-z; #2 -x+2,-y+1,-z+2; #3 x,y+1,z; #4 x,y-1,z

Table S4 Selected Hydrogen Bond Lengths (Å) and Bond Angles (°) of AMV-1

D-H...A	d(D-H)	d(H...A)	<D-H...A	d(D...A)	Symmetry
C6-H6...O19	0.930	2.304	127.47	2.963	
C9-H9...O20	0.930	2.449	120.67	3.031	[x-1, y, z]
C8-H8...O20	0.930	2.477	119.50	3.045	[x-1, y, z]
C10-H10...O11	0.930	2.652	152.00	3.501	[x-1/2, y+1/2, z]
C10-H10...O19	0.930	2.568	115.96	3.091	
C13-H13...O14	0.930	2.512	146.93	3.330	[x-1/2, -y+1/2, z+1/2]
C14-H14...O6	0.930	2.573	150.66	3.415	[x-1/2, -y+1/2, z+1/2]
C18-H18...O29	0.930	2.279	159.82	3.168	
C20-H20...O18	0.930	2.638	112.24	3.112	[x-1/2, -y+1/2, z+1/2]
C19-H19...O3	0.930	2.382	128.66	3.050	[x-1/2, y+1/2, z]

Table S5 Selected Hydrogen Bond Lengths (Å) and Bond Angles (°) of AMV-2

D-H...A	d(D-H)	d(H...A)	<D-H...A	d(D...A)	Symmetry
C2-H2...O33	0.930	2.507	138.93	3.266	[-x+1, y-1/2, -z+1/2]
C4-H4...O40	0.930	2.396	139.77	3.163	[-x+1, y-1/2, -z+1/2]
C7-H7...O18	0.930	2.651	121.36	3.234	[x, -y+3/2, z+1/2]
C8-H8...O2	0.930	2.637	143.29	3.428	[x, -y+5/2, z+1/2]
C10-H10...O38	0.930	2.532	123.09	3.138	

C11-H11...O37	0.930	2.361	147.03	3.182	[-x+2, -y+2, -z+1]
C12-H12...O2	0.930	2.359	162.18	3.257	[x, -y+5/2, z+1/2]
C13-H13...O5	0.930	2.282	136.12	3.022	[x, -y+3/2, z+1/2]
C14-H14...O10	0.930	2.547	137.57	3.294	[x, -y+5/2, z+1/2]
C15-H15...O39	0.930	2.480	167.43	3.394	[-x+1, y-3/2, -z+1/2]
C18-H18...O41	0.930	2.620	135.88	3.350	[x, -y+3/2, z+1/2]
C19-H19...O7	0.930	2.486	151.30	3.332	[x, -y+3/2, z+1/2]
C23-H23...O5	0.930	2.382	153.43	3.241	[x, -y+3/2, z+1/2]
C24-H24...O1	0.930	2.332	154.43	3.196	[x, -y+3/2, z+1/2]
C26-H26...O14	0.930	2.506	144.16	3.305	[x, y, z+1]
C27-H27...O23	0.930	2.448	123.45	3.061	[-x+2, y-1/2, -z+3/2]
C29-H29...O37	0.930	2.446	123.19	3.055	[x, y-1, z+1]
C30-H30...O10	0.930	2.473	144.09	3.272	[-x+2, y-1/2, -z+3/2]
C31-H31...O11	0.930	2.535	162.33	3.433	[-x+1, y-1/2, -z+1/2]
C32-H32...O21	0.930	2.479	119.56	3.047	[-x+1, y-1/2, -z+1/2]
C33-H33...O21	0.930	2.548	119.44	3.112	[-x+1, y-1/2, -z+1/2]
C33-H33...O35	0.930	2.532	134.75	3.254	
C35-H35...O19	0.930	2.286	152.06	3.138	[-x+1, y-1/2, -z+1/2]
C37-H37...O36	0.930	2.495	125.69	3.130	[x, -y+3/2, z+1/2]
C40-H40...O41	0.930	2.619	134.87	3.341	[x, -y+1/2, z+1/2]
C42-H42...O9	0.930	2.554	127.98	3.211	[x, -y+3/2, z+1/2]
C44-H44...O13	0.930	2.560	148.24	3.387	[x, -y+3/2, z+1/2]
C45-H45...O19	0.930	2.471	151.90	3.321	[x, -y+1/2, z+1/2]
C45-H45...O36	0.930	2.616	123.29	3.222	[-x+1, -y+1, -z+1]
O1W-H1WA...O26	0.850	2.482	162.45	3.302	
O1W-H1WB...N2	0.850	1.894	163.36	2.719	[x, y+1, z]
O2W-H2WB...O1W	0.850	2.316	122.61	2.865	[-x+1, y-1/2, -z+1/2]

Table S6. The Bond-valence Sums (BVS) for the Mo, As and Ag cations of AMV-1 and AMV-2.

Atoms	AMV-1	Oxidation state	AMV-2	Oxidation state
Mo1	5.752	+6	5.845	+6
Mo2	6.150	+6	6.035	+6

Mo3	5.613	+6	5.990	+6
Mo4	5.316	+5	6.191	+6
Mo5	5.868	+6	6.088	+6
Mo6	6.202	+6	6.037	+6
Mo7	6.250	+6	5.857	+6
Mo8	6.270	+6	6.026	+6
V1	4.614	+5	4.514	+5
V2	4.719	+5	4.650	+5
V3	4.538	+5	4.692	+5
V4	4.754	+5	4.625	+5
V5			4.240	+4
As1	5.191	+5	5.121	+5
As2	2.958	+3	2.600	+3
As3	2.580	+3		
Ag1			0.604	+1
Ag2			0.581	+1
Ag3			0.710	+1

4. Characterization

IR Analyses.

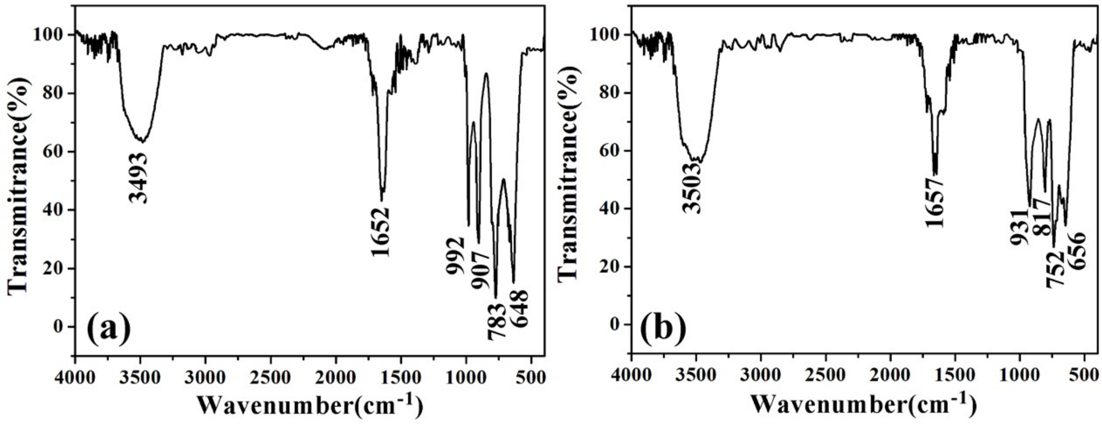

Figure S6. The IR spectra of AMV-1 (a) and AMV-2 (b).

The IR spectra of AMV-1 and AMV-2 between 4000 and 350 cm^{-1} were shown in Figure S6. The absorption peaks at 992, 907, 783, 648, cm^{-1} in AMV-1 and 931, 817, 752, and 656 cm^{-1} in AMV-2 can be attributed to the stretching vibration peaks of ν(M = O), ν(As-O-M) and ν(Mo-O-M) (M = V or Mo), respectively. The absorption peaks at 1300 and 1700 cm^{-1} in AMV-1 and 1300 and 1700 cm^{-1} in AMV-2 can be attributed to the stretching vibration peak of the organic ligand of two compounds, which is consistent with the crystal structure analysis.The broad peak at 3400-3600 cm^{-1} is caused by the stretching vibration spectrum ν(O−H) of water molecules.

TG Analyses.

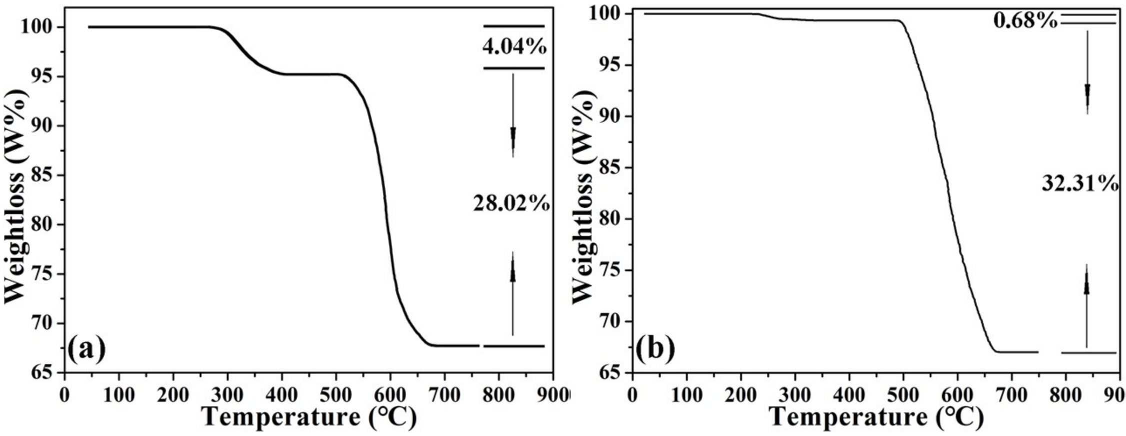

Figure S7. The TG curves of AMV-1 (a) and AMV-2 (b).

The TG curves of compounds AMV-1 and AMV-2 (Figure S7) were depicted under a N_2 atmosphere from 50 to 900 °C. Two obvious weight loss can be detected in the Figure S6a and b. The first weight losses of 4.04% (calcd 4.19%) at 260−390 °C for AMV-1, and 0.68% (calcd 0.65%) at 260−340 °C for AMV-2 can be attributed to the removal of all water molecules. The second weight losses of 28.02% (calcd 28.44%) at 390-670 °C for AMV-1, and 32.31% (calcd 32.58%) at 350-645 °C for AMV-2 are attributed to the losses of organic ligands bipy and As_2O_3.

XRD Analyses.

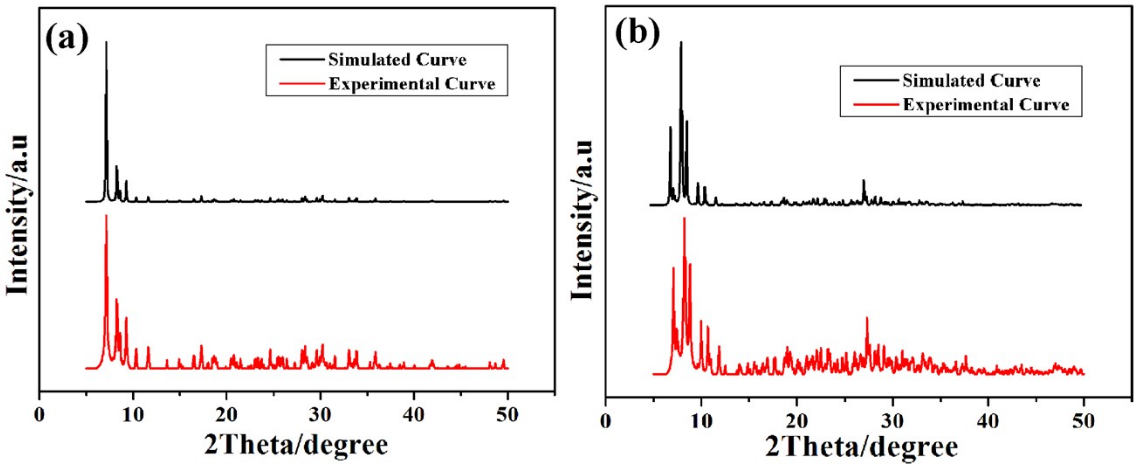

Figure S8. The XRD contrast curves of simulated and experimential for AMV-1 (a) and AMV-2 (b).

The XRD tests were performed on the powder samples of AMV-1 and AMV-2. The XRD contrast curves of simulated and experimental for two compounds were depicted in Figure S8. By comparing the experimental and simulated diffraction data, it is found that the characteristic peak positions of AMV-1 and AMV-2 basically coincide, indicating that two compounds have good crystallographic phase purity. However, the difference in the peak intensity of XRD may be caused by the different preferred orientation of a crystal surface caused by crystal dissociation during the sample preparation process.

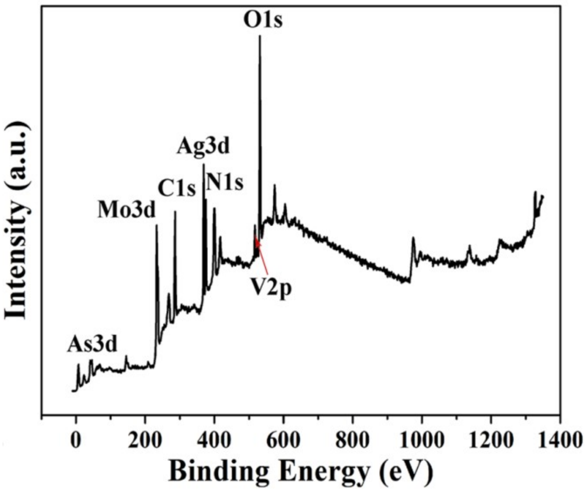

Figure S9. XPS total spectrum of AMV-2.

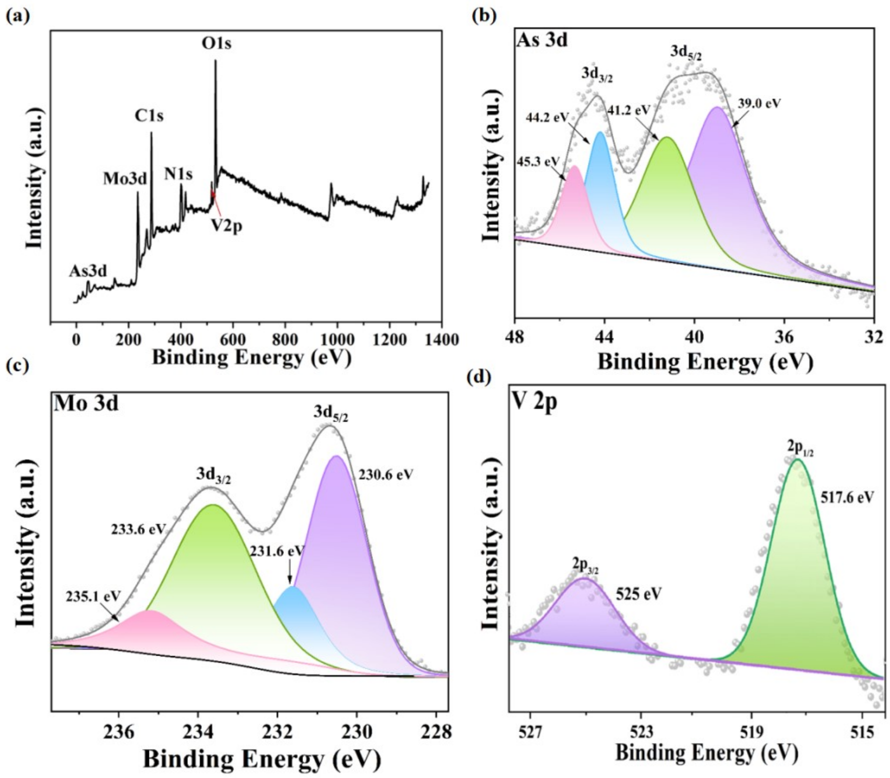

Figure S10. XPS of AMV-1: (a) total spectrum; (b) As 3d; (c) Mo 3d; (d) V 2p.

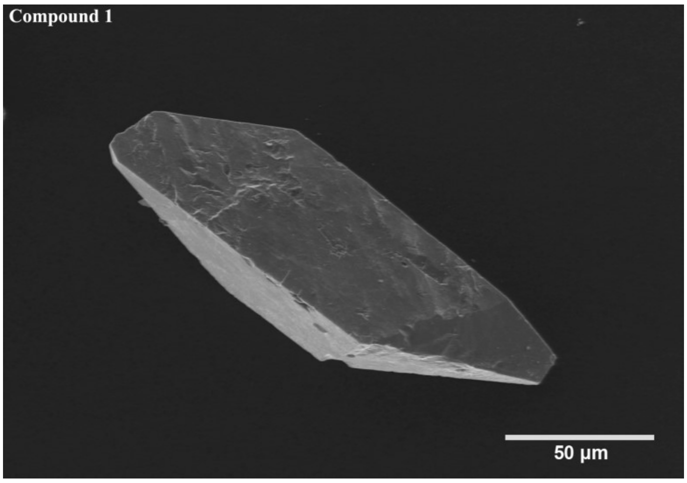

Figure S11. SEM image of AMV-1.

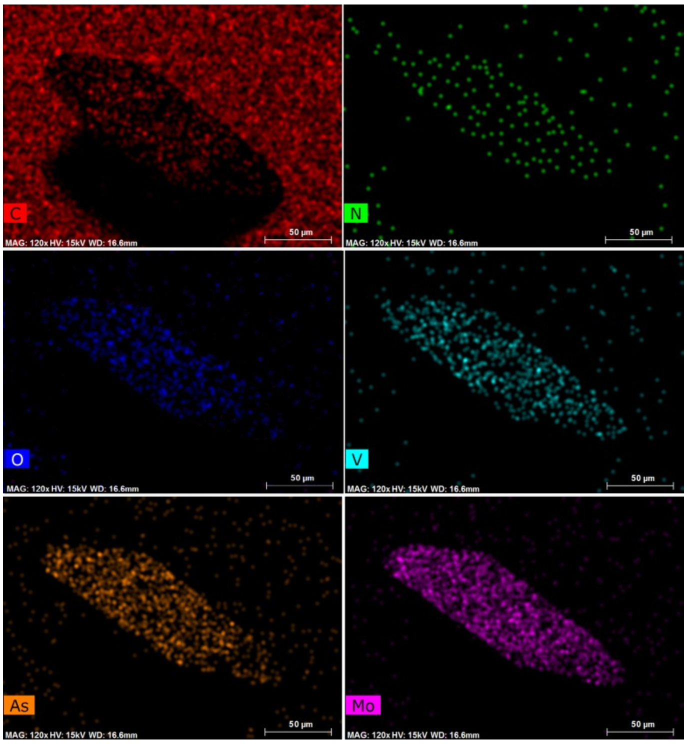

Figure S12. The EDS elemental mappings of As, Mo, V, C, O, and N, for AMV-1**.**

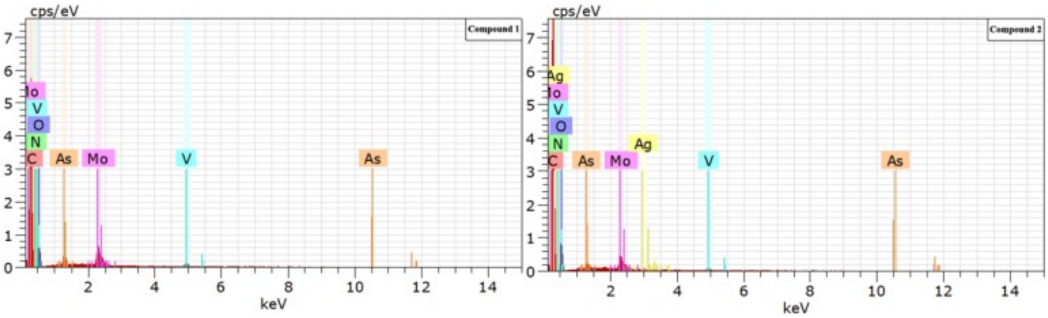

Figure S13. EDS image of AMV-1 and AMV-2**.**

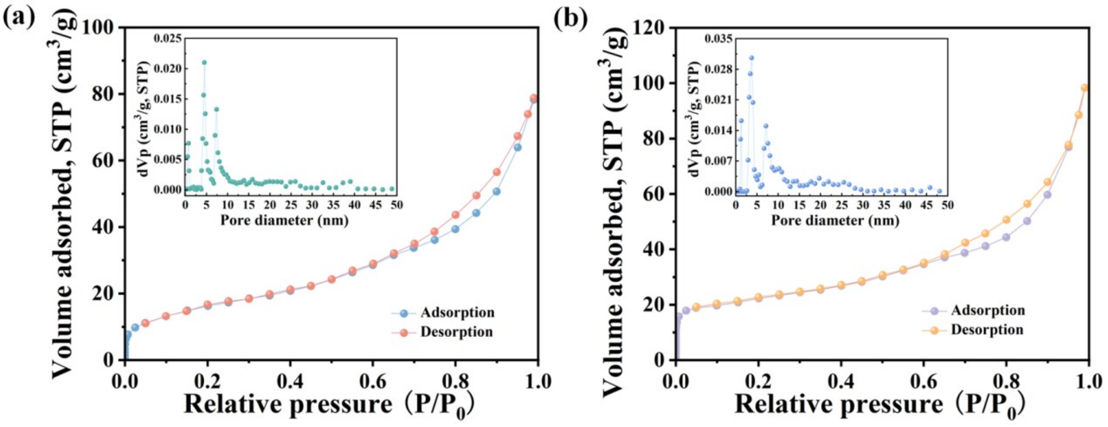

Figure S14. N_2 adsorption isotherms with corresponding pore-size distributions for AMV-1 and AMV-2**.**

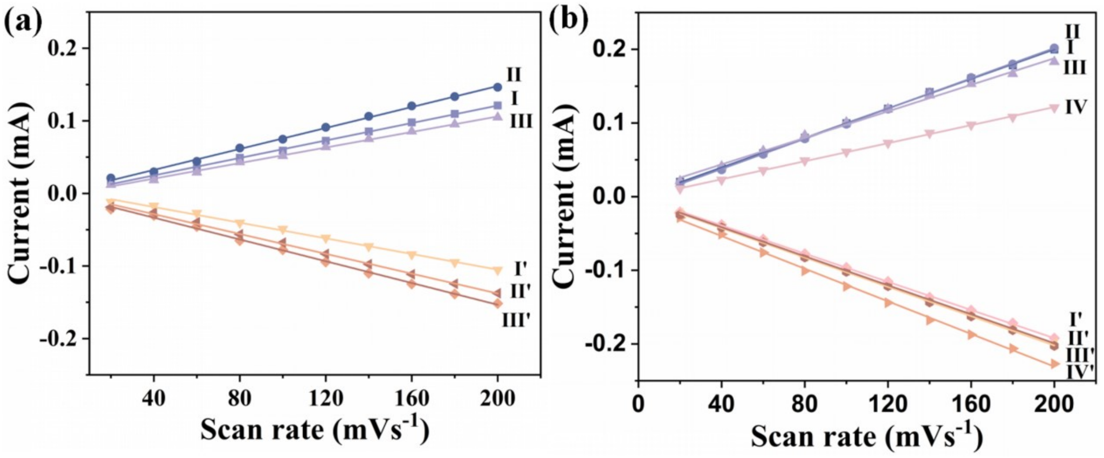

Figure S15. The plots of the anodic and cathodic peak currents vs scan rates for (a) AMV-1-GCE and (b) AMV-2-GCE.

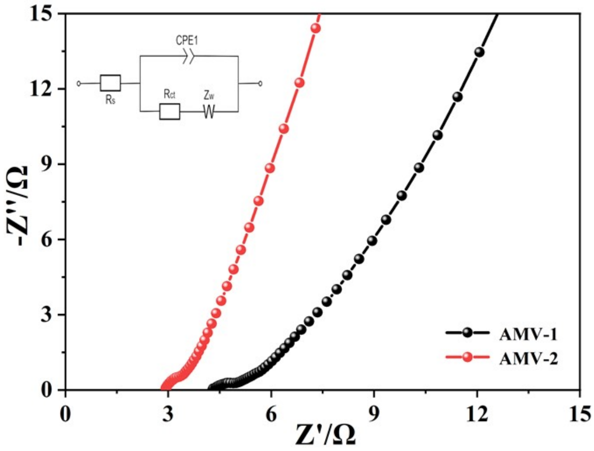

Figure S16. Nyquist plots of AMV-1-GCE and AMV-2-GCE.

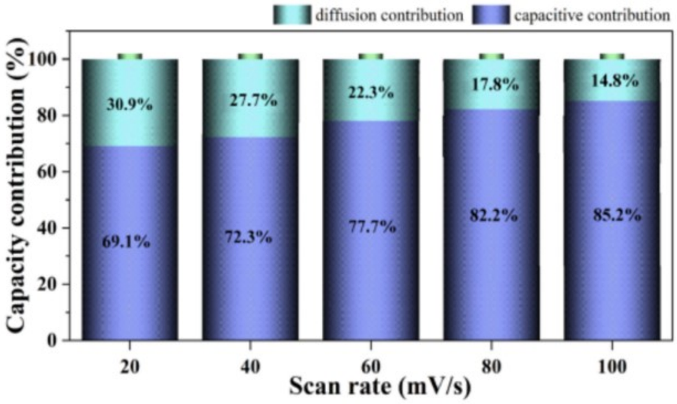

Figure S17. The contributions rate of two capacitive behaviors for AMV-2-CPE at different scanning rates.

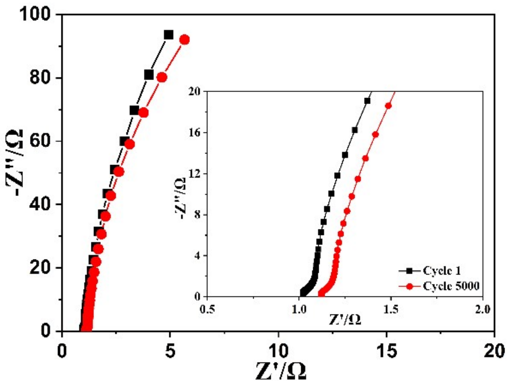

Figure S18. EIS spectra of AMV-2-CPE.

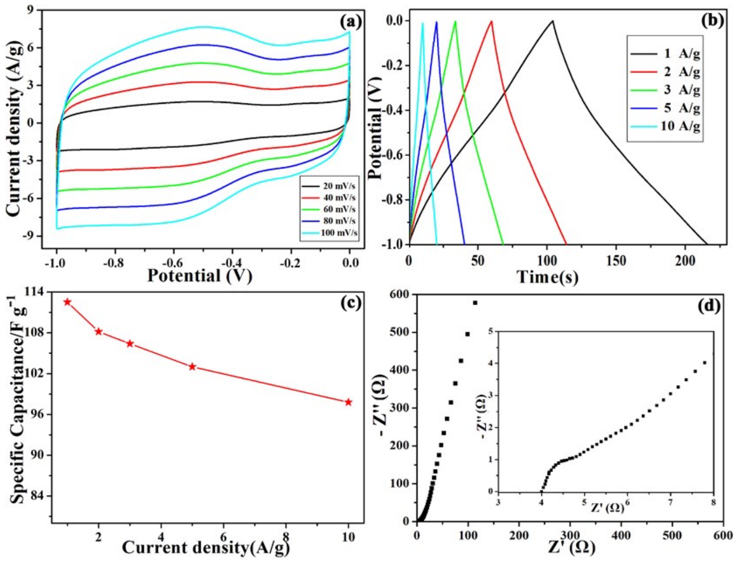

Figure S19. (a) The CV curves of AC-CPE at different scanning speeds (20-100 mV s^{-1}); (b) GCD of AC-CPE under diverse current densities; (c) The specific capacitance of AC-CPE at different current densities; (d) EIS spectra of AC-CPE (The inset shows a magnified part of the high-frequency range for the EIS spectra).

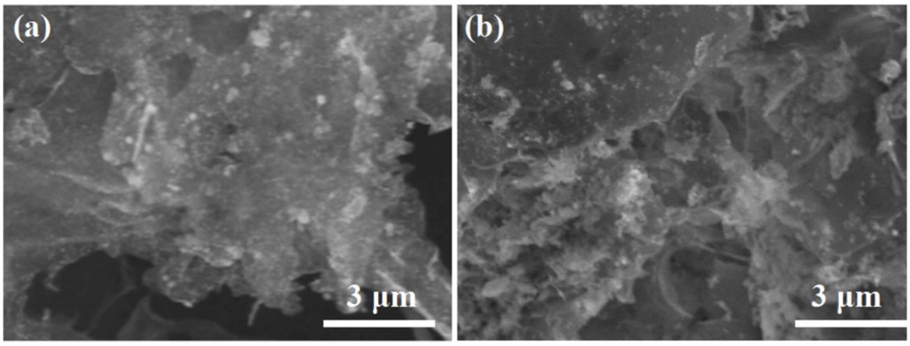

Figure S20. SEM images of the AMV-2-CPE electrode in ASC devices before and after GCD cycles.

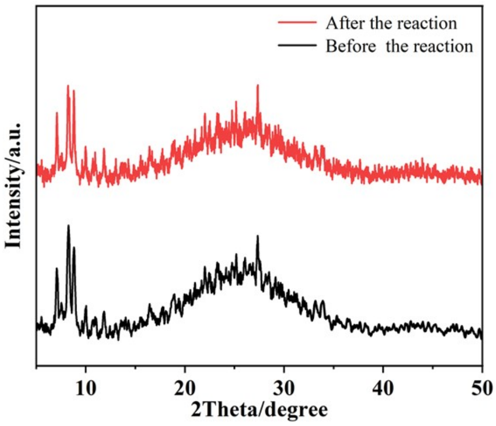

Figure S21. PXRD patterns of AMV-2-CPE befor and after the reaction.

Table S7 Performance comparison of aqueous supercapacitor devices with previously reported similar materials.

Supercapacitors	Energy density ($Wh\cdot kg^{-1}$)	Power density ($W\cdot kg^{-1}$)	normalization	Cyclic Stability	Capacities	Current density ($A\cdot g^{-1}$)	Ref
GO@MoPOM // MXene@WPOM	26.18	3646	2 mg/cm^{-2}	92.4% over 5000 cycles	110.4 $F\cdot g^{-1}$	1	[7]
PAN/gCD-MOF // PAN/gCD-MOF	17.5	6000	3 mg cm^2	97.5% over 6000 cycles	86.4 $F\cdot g^{-1}$	0.5	[8]
Co_4Ce_1-MOF//AC	44.18	775	/	98.4% over 5000 cycles	118.7 $F\cdot g^{-1}$	2	[9]
$\{PW_{12}\}$@SWNTs //$\{PW_{12}\}$@SWNTs	33.4	17600	1 mg cm^2	91.3% over 10000 cycles	240.6 $F\cdot g^{-1}$	1	[10]
Ni/Co-MOF//AC	29.5	199.1	2 mg cm^2	89% over 2000 cycles	80 F $F\cdot g^{-1}$	2	[11]
$[Mn(BGPD)(H_2O)_2]$ //rGO	35.5	0.79	3 mg/cm^{-2}	46.7% over 4000 cycles	100 $F\cdot g^{-1}$	1	[12]
$[Co(H_2bpap)(g\text{-}Mo_8O_{28})_{0.5}(H_2O)_2]H_2O$//$[Co(H_2bpap)(g\text{-}Mo_8O_{28})_{0.5}(H_2O)_2]H_2O$	13.4	450	1.25 mg/cm^{-2}	96% over 6500 cycles	102 $F\cdot g^{-1}$	1	[13]
ZADV@LSC// (ZADV@LSC	19.7	586	1 mg/cm^{-2}	89% over 5000 cycles	250.1 $F\cdot g^{-1}$	0.8	[14]
CuO@Ni-MOF//PAC-18	18	750	6-7 mg/cm^{-2}	94% over 5000 cycles	57.6 $F\cdot g^{-1}$	1	[15]
$(bipy)_{0.5}[\{Ag_2(bipy)_4\}\{(VO)(As^{III}AsMo_8V_4O_{40})\}]\cdot H_2O$//AC	37.2	1249.2	1 mg/cm^{-2}	92.8% over 10000 cycles	171.8 $F\cdot g^{-1}$	2	This work

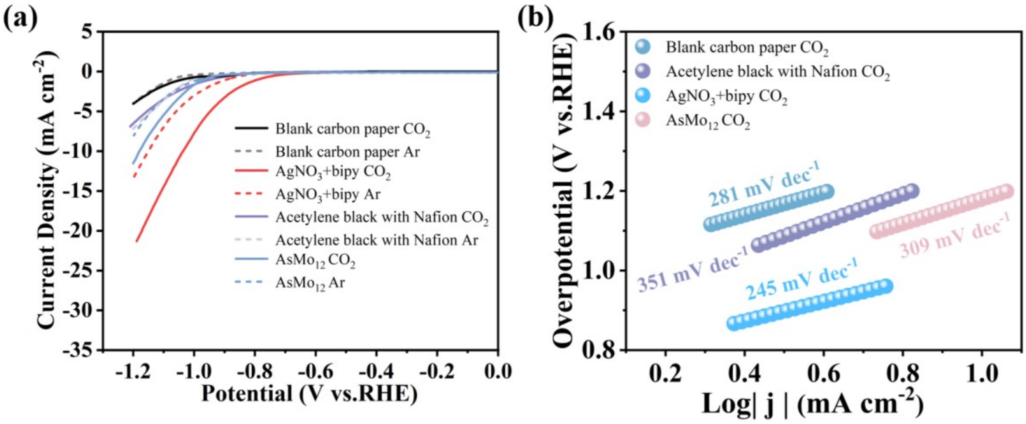

Figure S22. (a) Linear sweep voltammetric curves and (b) Tafel plot of different control samples.

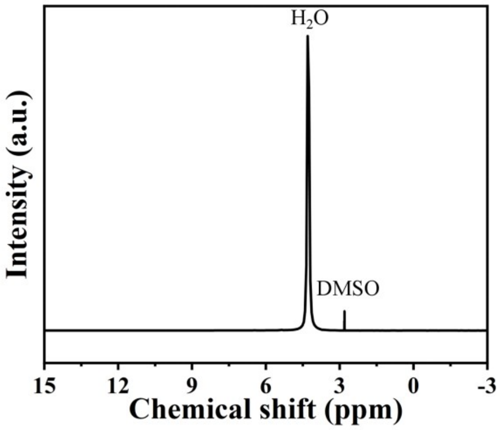

Figure S23. Characterization for the liquid product of AMV-2 during 3 h CO_2 reduction process by 1H nuclear magnetic resonance spectroscopy.

In this work, ^{1}H NMR measurements were performed using the electrolyte solution after electrolysis as the sample, with D_2O as the solvent and DMSO added as an internal standard. A solvent presaturation technique was employed to suppress the water signal. The experimental results show that no characteristic signals corresponding to liquid-phase carbon-based products, such as methanol or formic acid, were observed in the ^{1}H NMR spectra at any applied potential. Under the present experimental conditions, the detection limit of ^{1}H NMR for formate was approximately 32 μmol/L. Within this detection limit, no formate or other liquid-phase products were detected in the electrolyte after electrolysis, indicating that their formation, if any, is negligible compared to the gaseous products.

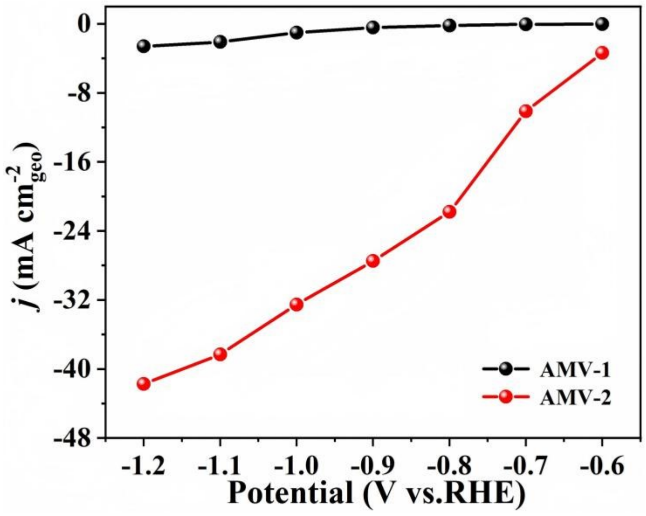

Figure S24. j_{CO} of AMV-1 and AMV-2.

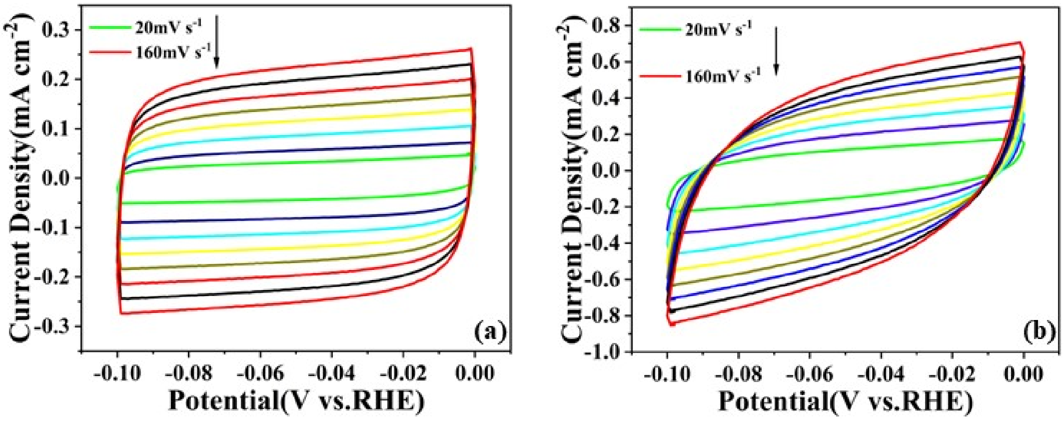

Figure S25. The CV curve of (a) AMV-1 and (b) AMV-2 in the potential range without redox current peaks.

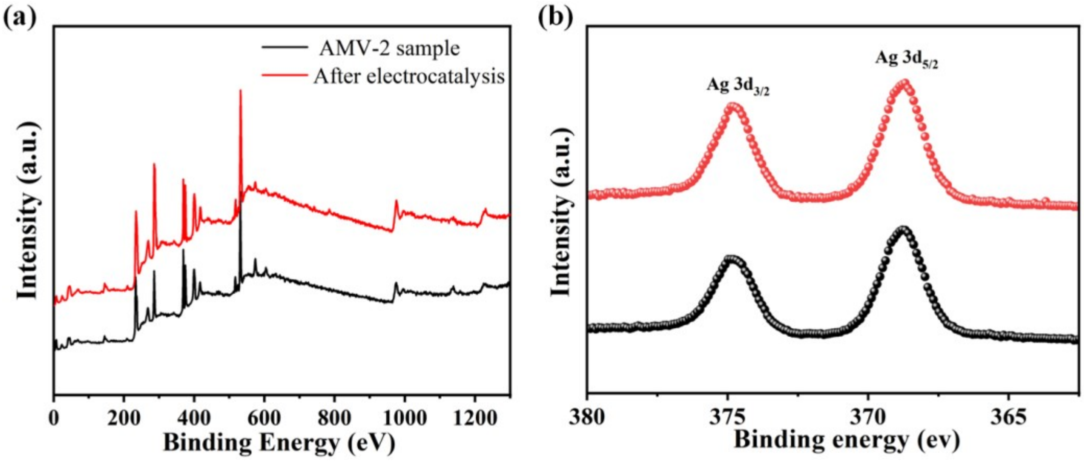

Figure S26. (a) XPS spectra and (b) high-resolution Ag 3d spectra of AMV-2 sample and after electrocatalysis.

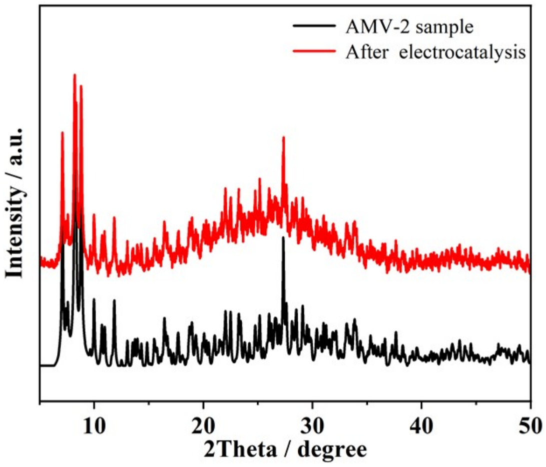

Figure S27. PXRD patterns of AMV-2 sample and after electrocatalysis.

5. Theoretical calculation

Initial geometric optimizations were executed in the ORCA computational suite[16]. These calculations incorporated the polarizable continuum model (PCM) to account for bulk aqueous solvation effects implicitly. The PBE0-D3 density functional served as the foundation for all electronic structure calculations: geometry optimizations leveraged the efficient Split-Valence plus Polarization (SVP) basis set, validated by convergence criteria, whereas final single-point energies were computed with the augmented Triple-Zeta Valence plus Polarization (TZVP) basis set to enhance accuracy[17,18]. Subsequent surface electrostatic potential analysis utilized Multiwfn software[19], with visualization performed in VMD[20].

In the computational section, we employed the PBE0 hybrid functional. The PBE0 functional mixes 25% exact Hartree-Fock exchange, 75% PBE exchange, and 100% PBE correlation. Unlike empirical functionals, its 25% mixing ratio is derived from fundamental theoretical arguments based on the adiabatic connection formalism, aiming for broader applicability. This choice was motivated by the intermolecular interactions and charge transfer involved in the reaction mechanism proposed in this study. Compared to pure functionals such as PBE, the inclusion of exact exchange in PBE0 allows for a more accurate description of electron delocalization in such processes, thereby providing more reliable predictions for the relative stability of adsorption intermediates. This has been confirmed by numerous benchmark studies on similar chemical systems[21].

For the treatment of solvent effects, we explicitly adopted the integral equation formalism of the polarizable continuum model (IEF-PCM) to simulate the experimental solvent environment.The primary reason is that the core experimental observations in this study, such as the stability of adsorption intermediates, are fundamentally driven by solvent stabilization of highly polar species.

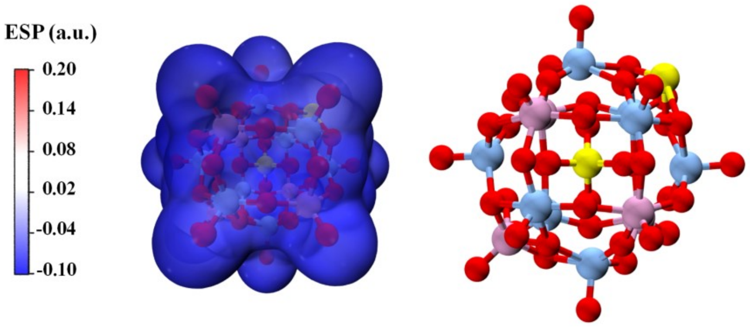

Figure S28. Electrostatic potential of $\{(VO)\{As^{III}AsMo_8V_4O_{40}\}$ cluster.

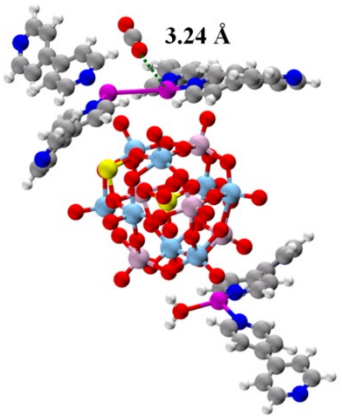

Figure S29. Ag···O=C=O adsorption configuration of AMV-2.

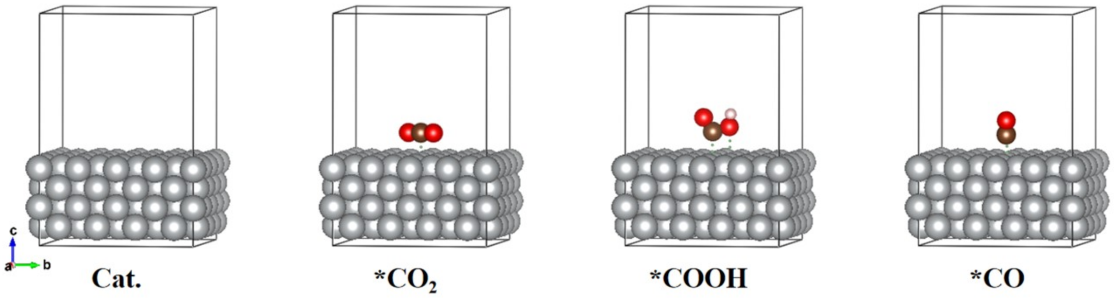

Figure S30. Proposed reaction pathway for CO production via electrocatalytic CO_2RR on pure Ag surface.

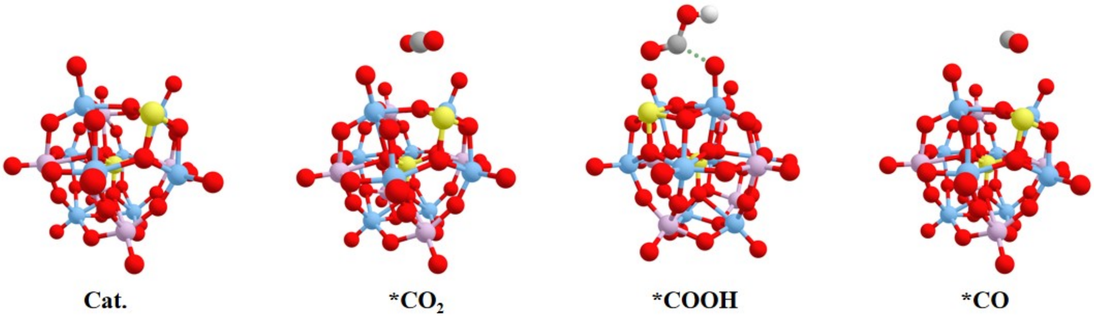

Figure S30. Proposed reaction pathway for CO production via electrocatalytic CO_2RR on {(VO){$As^{III}AsMo_8V_4O_{40}$} cluster.

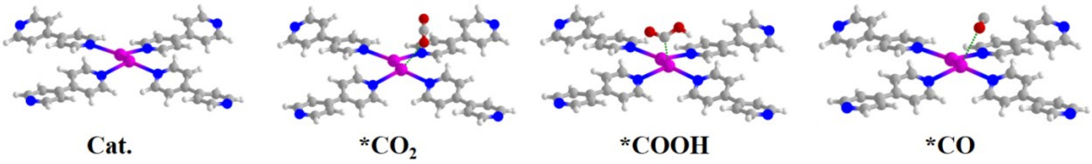

Figure S31. Proposed reaction pathway for CO production via electrocatalytic CO_2RR on {Ag_2(bipy)$_4$} unit.

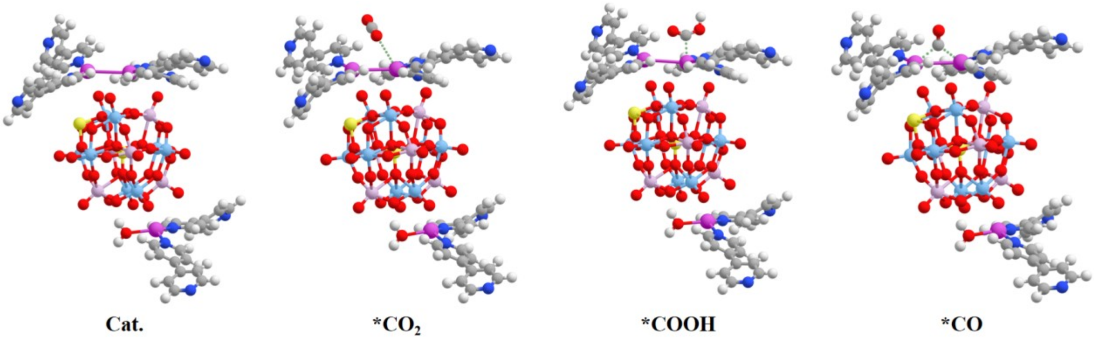

Figure S32. Proposed reaction pathway for CO production via electrocatalytic CO_2RR on AMV-2.

References

(1) Roy, S.; Vemuri, V.; Maiti, S.; Manoj, K. S.; Subbarao, U.; Peter, S. C. Two Keggin-Based Isostructural POMOF Hybrids: Synthesis, Crystal Structure, and Catalytic Properties. Inorganic chemistry. 2018, 57, 12078-12092.

(2) Wang, G. N.; Chen, T. T.; Li, S. B.; Pang, H. J.; Ma, H. Y. A coordination polymer based on dinuclear (pyrazinyl tetrazolate) copper(II) cations and Wells-Dawson anions for high-performance supercapacitor electrodes. Dalton Transactions. 2017, 46,

13897-13902.

(3) Wang, C. L.; Rong, S.; Zhao, Y. Q.; Wang, X. M.; Ma, H. Y. Three-dimensional supramolecular crystalline materials based on Keggin-based polyoxometalates and 1,2-Bis (4-pyridyl) ethylene for supercapacitor electrodes. Transition Metal Chemistry. 2021, 46, 335-343.

(4) Guo, D. X.; Zhou, C. L.; Tan, L. C.; Ma, H. Y.; He, R. R.; Pang, H. J.; Wang, X. M. Electrochemical ascorbic acid sensor of composite film based on Keggin-type Vanadium-substituted Polyoxometalates decorated with graphene and $Ru(bpy)_3^{2+}$. J. Colloids and Surfaces A: Physicochemical and Engineering Aspects. 2020, 592, 124550.

(5) Liu, X. Z.; Cui, L. P.; Yu, K.; Lv, J. H.; Liu, Y. H.; Ma, Y. J.; Zhou, B. B. Cu/Ag Complex Modified Keggin-Type Coordination Polymers for Improved Electrochemical Capacitance, Dual-Function Electrocatalysis, and Sensing Performance. Inorganic chemistry. 2021, 60, 14072-14082.

(6) Ma, X. Y.; Yu, K.; Yuan, J.; Cui, L. P.; Lv, J. H.; Dai, W. T.; Zhou, B. B. Multinuclear Transition Metal Sandwich-Type Polytungstate Derivatives for Enhanced Electrochemical Energy Storage and Bifunctional Electrocatalysis Performances. Inorganic Chemistry. 2020, 59, 5149-5160.

(7) A. Das, M. Mohapatra, S. Basu, Unleashing asymmetric polyoxometalate redox activators on 2D interfaces for high-performance hybrid energy storage. Carbon, 2024, 223, 119007.

(8) W. Xu, L. H. Wang, Y. Chen, Y. Liu, Flexible carbon membrane supercapacitor based on γ-cyclodextrin-MOF. Materials Today Chemistry, 2022, 24, 100896.

(9) H. M. Lan, Y. X. Hu, Q. T. Liu, B. H. Wu, F. Yu, T. T. Gu, W. Guo, Y. Y. Liu, Improving the supercapacitor performance of the Co-MOF via cerium-induced shape modulation and defect engineering. Materials Chemistry Frontiers, 2025, 9, 2694-2703.

(10) S. Zhu, X. X. Yang, Y. X. Yao, X. R. Zhang, L. Li, X. Wang, G. Y. Han, Y. Li, One-dimensional heterostructures of polyoxometalate-encapsulated carbon nanotubes

for enhanced capacitive energy storage. Cell Reports Physical Science, 2023, 4,101446.

(11) X. Mao, H. Liu, T. Niu, X. Yan, M. Li, TEA Guiding Bimetallic MOF with Oriented Nanosheet Arrays for High-Performance Asymmetric Supercapacitors. Polymers, 2024, 16, 3198.

(12)H. R. Rong, P. Song, G. X. Gao, Q. Y. Jiang, X. J. Chen, L. X. Su, W, L, Liu, Q. Liu, A three-dimensional Mn-based MOF as a high-performance supercapacitor electrode. Dalton Trans., 2023, 52, 1962-1969.

(13) X. L. Wang, J.J. Lu, H. Y. Lin, Q. Q. Liu, K. K. Chen, Polyoxometalate-based metal－organic supramolecular architectures derived from two new pyrimidine-amide ligands as supercapacitors and multifunctional electrochemical sensors, New J. Chem., 2023, 47,17051-17059.

(14) D. Kumar, A. Joshi, G. Singh, R.K. Sharma, Polyoxometalate/ZIF-67 composite with exposed active sites as aqueous supercapacitor electrode. Chemical Engineering Journal, 2022, 431, 134085.

(15) S. Kumar, P. H. Weng, Y. P. Fu, Core-shell-structured CuO@Ni-MOF: bifunctional electrode toward battery-type supercapacitors and oxygen evolution reaction. Materials Today Chemistry, 2022, 26, 101159.

(16) Neese, F. The ORCA program system. Wiley Interdisciplinary Reviews: Computational Molecular Science. 2012, 2, 73-78.

(17)Becke, A. D. A new mixing of Hartree-Fock and local density-functional theories. J. Chem. Phys. 1993, 98, 1372-1377.

(18) Weigend, F. & Ahlrichs, R. Balanced basis sets of split valence, triple zeta valence and quadruple zeta valence quality for H to Rn: Design and assessment of accuracy. Phys. Chem. Chem. Phys. 2005, 7, 3297-3305.

(19) Lu, T. & Chen, F. Multiwfn: A multifunctional wavefunction analyzer. J. Comput. Chem. 2012, 33, 580-592.

(20)Humphrey, W., Dalke, A. & Schulten, K. VMD: Visual molecular dynamics. J. Mol. Graph. 1996, 14, 33-38.

(21) Li, H., Xu, L., Bo, S. et al. Ligand engineering towards electrocatalytic urea synthesis on a molecular catalyst. Nat Commun, 2024, 15, 8858.